RSC Advances




ROYAL SOCIETY OF CHEMISTRY

www.rsc.org/advances

## The image for TOC

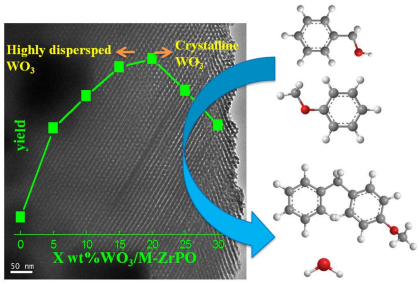


A series of $WO_3$ supported on ordered mesoporous zirconium oxophosphate solid acid catalyst was employed in benzylation reaction.

# Ordered mesoporous zirconium oxophosphate supported tungsten oxide solid acid catalysts: the improved Brønsted acidity for benzylation of anisole

Zhichao Miao[a,b], Huahua Zhao[a], Huanling Song[a,c], Lingjun Chou[a,c*]

**Abstract**

A series of $WO_3$ supported on the ordered mesoporous zirconium oxophosphate (X wt%$WO_3$/M-ZrPO) solid acid catalysts with $WO_3$ loading from 5 to 30 wt% were successfully synthesized, and their structure properties were characterized by X-ray diffraction (XRD), Raman spectroscopy, $N_2$-physisorption, transmission electron microscopy (TEM), UV-visible diffuse reflectance spectra, Fourier transform infrared (FT-IR) spectra, $H_2$ temperature-programmed reduction ($H_2$-TPR) and X-ray photoelectron spectroscopy (XPS). The catalytic performance of X wt%$WO_3$/M-ZrPO in liquid phase benzylation of anisole was studied and the relation between activity and states of tungsten species was investigated detailedly. The maximum catalytic activity was reached at a 20 wt% $WO_3$ loading, which possessed highly dispersed $WO_3$ species and strongest Brønsted acidity. Meanwhile, the well dispersed $WO_3$ species strongly interacted with M-ZrPO, therefore, both sintering and leaching of $WO_3$ species were effectively restrained. Moreover, compared with the traditional zirconium phosphate synthesized from sol-gel method ($ZrP_{sol\text{-}gel}$), the M-ZrPO with abundant ordered mesostructure was propitious for improving the dispersion of $WO_3$ species and catalytic performance. In addition, the 20 wt%$WO_3$/M-ZrPO showed a markedly higher catalytic activity than H-ZSM5, H-Beta and 20 wt%$WO_3$/$ZrP_{sol\text{-}gel}$.

Furthermore, the catalyst showed no discernible loss in activity or selectivity after five cycles.

**Keywords:** mesoporous materials, solid acid catalyst, improved Brønsted acidity, FC benzylation.

## 1. Introduction

Supported tungsten oxide catalysts were a class of important heterogeneous catalysts and widely utilized in many reactions, such as, metathesis and isomerization of alkenes,[1-4] selective oxidation of hydrocarbon,[5-7] selective reduction of nitric oxide with ammonia,[8-11] hydrodesulfurization and hydrocracking of heavy fractions in the petroleum chemistry.[12-15] During these applications, the tungsten oxide-based catalysts have attracted vast attention in the field of solid acid catalysts.[16-18] Compared with traditional homogeneous liquid acid catalysts, novel heterogeneous solid acid catalysts should be encouraged due to the high reactivity, no corrosion, friendly to environment and easy to recover and reuse.[19-20] Owing to their excellent acidic property, stability and regenerability, the tungsten oxide-based catalysts, such as $WO_3/Al_2O_3$,[21-22] $WO_3/TiO_2$,[23] $WO_3/SiO_2$,[24] $WO_3/ZrO_2$,[25-27] tungsten oxide supported on metal sulfates and phosphates,[28-32] were widely employed as solid acid catalyst and exhibited superior catalytic performance in hydrolysis of cellulose, synthesis of biodiesel, Beckmann rearrangement of cyclohexanone oxime, isomerization of alkane and dehydration of alcohols. In addition, different influence factors, such as the dispersion, oxidation state, surface acidity and structure, largely influence the catalytic performance of tungsten based solid acid catalysts in these reactions.[6,26]

Since the first mesoporous molecular sieve MCM-41 was successfully synthesized in 1992,[33-34] different kinds of mesoporous materials have been developed. Owing to the outstanding textural properties, mesoporous materials have been widely employed as catalysts and supports in the field of catalysis.[35-36] Compared with the traditional

supports, mesoporous materials possess larger specific surface area, bigger pore volume and more ordered pore channels, which allow the active component highly dispersed on the support to provide more additional active sites for the reactant molecules resulting in improved catalytic performance.[37-38] Therefore, mesoporous materials, especially non-silica mesoporous materials like metal oxides and metal composite oxides, promise a series of potential carriers and have attracted growing interest in the field of catalysis. In addition, mesoporous materials supporting tungsten oxide have drawn considerable attention because of their diverse compositions that lead to potential applications in solid acid catalysis.[39-40] However, the reports about tungsten oxide supported on non-silica based ordered mesoporous materials are very few and have potential to be investigated.

In this paper, a series of $WO_3$ loaded on the ordered mesoporous zirconium oxophosphate (M-ZrPO) with different $WO_3$ loading was prepared through ultrasonic impregnation strategy and employed as solid acid catalyst in the Friedel-Crafts (FC) benzylation reactions. FC benzylation is one of the fundamental organic reactions for preparation of fine chemicals, dielectric fluids and pharmaceutical chemicals.[41] Compared with traditional homogeneous catalysts, solid acid catalysts should be encouraged to utilize in the benzylation reactions.[42-44] To gain more insight into the possible relation between structure and catalytic properties, the present work systematically characterized X wt%$WO_3$/M-ZrPO by $N_2$-physisorption and TEM for the mesoporous properties of materials, XRD, Raman, UV-vis, FT-IR, $H_2$-TPR and XPS spectroscopy for the states of tungsten species in the materials as well as

$NH_3$-TPD and Pyridine-IR analyses for acidic property. In addition, the influences of tungsten species on Brønsted acidic property and catalytic activity of X wt%$WO_3$/M-ZrPO were discussed detailedly. Furthermore, the catalytic performance of 20 wt%$WO_3$/M-ZrPO was compared with conventional solid acids (H-Beta and H-ZSM5) and $WO_3$ loaded on the $ZrP_{sol\text{-}gel}$ which was synthesized from sol-gel method.

## 2. Experimental Section

### 2.1 Catalyst preparation.

$(EO)_{106}(PO)_{70}(EO)_{106}$ triblock copolymer (Pluronic F127, $M_{av}$ = 12600, Sigma-Aldrich), zirconyl chloride octahydrate ($ZrOCl_2 \cdot 8H_2O$, ≥99.0%, Tianjin Fengyue Reagent Company), trimethyl phosphate ($PO(OCH_3)_3$, ≥99.0%, Sinopharm Chemical Reagent Co. Ltd.), ammonium tungstate ($(NH_4)_5H_5[H_2(WO_4)_6] \cdot H_2O$, ≥99.0%, Sinopharm Chemical Reagent Co. Ltd.), ethanol (≥99.7%, Sinopharm Chemical Reagent Co. Ltd.). All the reagents are A.R. grade and used as received without further purification.

Ordered mesoporous zirconium oxophosphate (M-ZrPO) was synthesized via improved one-pot evaporation-induced self-assemble (EISA) strategy as reported in previous report.[45] In a typical procedure of synthesizing M-ZrPO, 1.2 g of F127 (employed as structure-directing agents (SDAs)) were dissolved in 15 mL of anhydrous ethanol. As the SDAs were completely dissolved, 5 mmol of $ZrOCl_2 \cdot 8H_2O$ and 3.75 mmol of $PO(OCH_3)_3$ (the molar ratio of P/Zr was 0.75) were added into the

above solution with vigorous stirring. The final solution was covered with PE film and stirred at least for 6 h. Finally, the transparent solution mixture was transferred to a petri dish (d=9 cm) to undergo the slow EISA process at 60 $^{o}$C for 48 h, 100 $^{o}$C for 24 h in a drying oven. The obtained colorless and transparent xerogel was calcined by slowly increasing temperature (1 $^{o}$C/min ramping rate) to 550 $^{o}$C and kept at the final temperature for 5 h to remove the SDAs. The obtained template-free self-assembled mesoporous zirconium oxophosphate was denoted as M-ZrPO.

The amorphous zirconium phosphate synthesized from sol-gel method ($ZrP_{sol\text{-}gel}$) was as reported by Al-Qallaf *et al*.[46] $H_3PO_4$ and $ZrOCl_2{\cdot}8H_2O$ were employed as the source and the molar ratio of P/Zr (0.75) was kept consistent with the M-ZrPO.

The supported $WO_3$ solid acid catalysts were prepared via incipient wetness impregnation method assisted with 3 h ultrasound treatment with ammonium tungstate as the precursor of $WO_3$. After impregnation, the catalyst precursors were dried under irradiation of infrared lamp and then dried at 120 $^{o}$C for 12 h. Finally, the catalyst precursors were calcined at 500 $^{o}$C for 5 h. The obtained catalysts were denoted as X wt%$WO_3$/M-ZrPO and X wt% (X wt% = $m_{WO3}/(m_{WO3}+m_{M\text{-}ZrPO})\times$ 100%) stood for the $WO_3$ loading.

**2.2 Characterization.**

Powder X-ray diffraction (XRD) measurements were performed using an X'Pert Pro Multipurpose diffractometer (PANalytical, Inc.) with Cu Kα radiation (0.15406 nm) at room temperature from 0.6° to 5.0° (small angle) and 10.0° to 80.0° (wide

angle). Measurements were conducted using a voltage of 40 kV, current setting of 20 mA for small angle XRD (SXRD) and 40 mA for wide angle XRD (WXRD), step size of 0.02°, and count time of 4 s.

The Raman spectra were recorded on a Laboram 010 confocal Raman System (Horiba JobinYvon, France) equipped with 632 nm He-Ne laser.

The nitrogen adsorption and desorption isotherms at -196 $^{o}$C were recorded on an Autosorb-iQ analyzer (Quantachrome Instruments U.S.). Prior to the tests, all the samples were pretreated at 200 $^{o}$C for 2 h. The specific surface areas were calculated via the Brunauer-Emmett-Teller (BET) method in the relative pressure range of 0.05-0.3; the single-point pore volume was calculated from the adsorption isotherm at a relative pressure of 0.990; pore size distributions were calculated using adsorption branches of nitrogen adsorption-desorption isotherms by Barrett-Joyner-Halenda (BJH) method. The tungsten surface densities expressed as the number of W atoms per nanometer square area (W atoms·nm$^{-2}$) and were calculated using the equation: Surface density of W = {[$WO_3$ loading (wt%)/100]$\times$6.023$\times$10$^{23}$}/{[231.8 (formula weight of $WO_3$)$\times$$S_{BET}$ ($m^2 \cdot g^{-1}$)$\times$10$^{18}$]}.[47]

Transmission electron microscopy (TEM) images and energy-dispersive X-ray spectroscopy (EDX) measurements were performed on the TECNAI G$^2$ F20 high-resolution transmission electron microscopy under a working voltage of 200 kV.

UV-visible diffuse reflectance spectra were recorded on a PE Lambda 650S in the range of 190-800 nm.

Fourier transform infrared (FT-IR) spectra were recorded on KBr pellets by a

Nexus 870 infrared spectrometer with the wave number from 4000 to 400 $cm^{-1}$.

X-ray photoelectron spectroscopy (XPS) analysis of the samples was performed on a Thermon Scientific ESCALAB250xi spectrometer. All binding energies were calibrated to the $C_{1s}$ line (284.8 eV).

$H_2$ temperature-programmed reduction ($H_2$-TPR) measurements were performed on an AMI-100 unit (Zeton-Altamira instrument) employing $H_2$ gas as reducing agent. The samples (0.1 g) were loaded in a U-shaped quartz reactor. Prior to TPR measurements, the samples were pretreated at 200 $^oC$ for 1 h in flowing He gas (50 $mL \cdot min^{-1}$) to remove any moisture and other adsorbed impurities. After cooling the reactor to room temperature, a 5% $H_2$-He gas (50 $mL \cdot min^{-1}$) mixture was introduced. The catalyst was heated to 1100 $^oC$ at a rate of 20 $^oC \cdot min^{-1}$ and the $H_2$ gas consumption was measured using an AMETEK (LC-D-200 Dycor AMETEK) mass spectrometer.

Temperature programmed desorption of ammonia ($NH_3$-TPD) was performed on the same instrument as reported in $H_2$-TPR. A typical experiment for the TPD measurement was as follows: the sample (0.1 g) was pretreated at 200 $^oC$ for 1 h in the flowing He gas to remove any moisture and absorbed impurities. After cooling to 100 $^oC$, 10 mol% $NH_3$-He gas (50 $mL \cdot min^{-1}$) was introduced for 30 min. Physically absorbed $NH_3$ was then removed completely by desorbing in He gas at 100 $^oC$ (observed from the mass spectrometer signal). The TPD experiment was then carried out by raising the temperature of sample in a programmed manner (10 $^oC \cdot min^{-1}$) to 700 $^oC$.

The infrared spectra of adsorbed pyridine (Pyridine-IR) were recorded on PE Frontier FT-IR spectrometer. The sample (~15 mg) was pressed into a pellet (~13 mm), activated at 400 $^{o}$C for 1 h under vacuum, then cooled to room temperature and pyridine was introduced and adsorbed for 30 min. The sample was raised to a desired temperature and held for 30 min under vacuum, after which the spectra was recorded. The blank experiments were operated under the same conditions and used as the background to insure the accuracy of the infrared spectra of adsorbed pyridine. The Brønsted and Lewis acidity was determined by the method proposed by Emeis.[48]

**2.3 Catalytic Reaction.**

Liquid phase Friedel-Crafts (FC) benzylation of anisole with benzyl alcohol was performed in a three-necked round bottom flask coupled with a reflux condenser in a temperature controlled oil bath as reported by Rao *et al*.[35] In a typical run, 0.2 g of X wt%$WO_3$/M-ZrPO was added to a mixture of anisole (20 mL) and benzyl alcohol (2 mL) with dodecane (0.4 mL) used as an internal standard for gas chromatography (GC) analysis. Nitrogen was introduced into the flask through one of the gas inlets. The reaction was carried out at 170 °C under reflux condition and with vigorous stirring for 2 h. The conversion of benzyl alcohol and selectivity of products were monitored by a gas chromatography (GC) instrument (Agilent-7890A; equipped with a flame ionization detector (FID) and HP-5 column (30 m × 0.32 mm × 0.25 μm)). Gas chromatography-mass spectroscopy (GC-MS) instrument (5975c vl MSD with triple-axis detector, GC Agilent-7890A) was employed to identify the reaction products. After completion of the reaction, the catalyst was separated by

centrifugation and activated at 400 $^{o}$C for 3 h for regeneration.

## 3. Results and discussion

### 3.1 Structure characterization of support M-ZrPO material.

As our previous report, the M-ZrPO possessed ordered mesostructure.[45] Shortly, as shown in Fig. 1(1), obvious diffraction peaks in SXRD pattern could be clearly found, implying the existence of ordered mesopores. In addition, there were only two broad peaks in WXRD pattern, showing the pore wall structure was amorphous. Moreover, the typical H1-type hysteresis loop, narrow pore size distribution (Fig. 1(2)) and TEM images (Fig. 2) further confirmed the existence of ordered pores in M-ZrPO.

**Figure 1**

**Figure 2**

### 3.2 Characterization of the as-prepared X wt%$WO_3$/M-ZrPO

#### 3.2.1 XRD and Raman analysis

The WXRD patterns of X wt%$WO_3$/M-ZrPO solid acid catalysts are shown in Fig. 3. As shown in Fig. 3(1), the patterns exhibited similar profile to M-ZrPO, only presenting two broad peaks in the WXRD patterns as $WO_3$ loading was under 20 wt%. The absence of typical peaks of crystalline $WO_3$ implied that tungsten species existed as highly dispersed state on the M-ZrPO surface in these samples. However, the weak peaks at 22-25$^{o}$ (23.1$^{o}$, 23.5$^{o}$, 24.3$^{o}$ shown in Fig. 3(2)), 34$^{o}$, 51$^{o}$ and 56$^{o}$, which could be indexed to monoclinic $WO_3$ (JCPDS card no. 89-4476), began to appear on 25

wt%$WO_3$/M-ZrPO sample, suggesting that some of tungsten species congregated on the surface to form crystalline $WO_3$. Further increase $WO_3$ loading to 30 wt%, much enhanced intensity of diffraction peaks from crystalline $WO_3$ could be observed, illustrating that more tungsten species agglomerated and formed crystalline $WO_3$. Moreover, the color of X wt%$WO_3$/M-ZrPO changed from white to slight yellow at high $WO_3$ loading (≥ 25 wt%), which was a qualitative indication for the formation of crystalline $WO_3$.[49] However, the crystallite size of $WO_3$ was still difficult to be calculated by Scherrer equation due to the peak broadening in the WXRD patterns. This might imply that no obvious crystalline $WO_3$ particles existed in 25 wt%$WO_3$/M-ZrPO and 30 wt%$WO_3$/M-ZrPO.

Moreover, Raman spectra were employed to further identify the major structural information concerning surface tungsten oxide species. As shown in Fig. 4, the bulk $WO_3$ showed obvious bands at 725 and 815 $cm^{-1}$, which were assigned to the W=O bending and stretching modes in the crystalline $WO_3$ species.[26,50] However, with $WO_3$ loading between 5 and 20 wt%, there were no distinct bands in the spectra, implying that no crystalline $WO_3$ existed in these samples. Further increasing $WO_3$ loading to 25 and 30 wt%, weak Raman bands could be observed at 725 and 815 $cm^{-1}$. This might be due to the agglomeration of microcrystalline $WO_3$ on the surface of the 25 wt%$WO_3$/M-ZrPO and 30 wt%$WO_3$/M-ZrPO. However, these bands were quite weak, implying the $WO_3$ species with low crystallinity existed in the two samples. Therefore, Raman results further confirmed what were previously observed by WXRD. Consequently, in the 5-20 wt%$WO_3$/M-ZrPO samples, the tungsten species were

highly dispersed on the support, whereas, the content surpassed threshold of mono-dispersed state and crystalline $WO_3$ began to appear on the surface of M-ZrPO as $WO_3$ loading reached 25 and 30 wt%.[51]

**Figure 3**

**Figure 4**

### 3.2.2 Nitrogen adsorption-desorption analysis

The nitrogen adsorption-desorption isotherms as well as pore size distributions of X wt%$WO_3$/M-ZrPO samples are displayed in Fig. 5. As shown in Fig. 5(1), all samples presented typical IV type isotherm with H1 shaped hysteresis loops, proving the successful preservation of mesostructure. Besides, all catalysts performed extremely narrow pore size distribution around 5.6 nm. In contrast with the M-ZrPO support, their average pore diameter did not change largely, indicating that the loaded $WO_3$ did not cause significant plugging of mesoporous pores even in 25 wt%$WO_3$/M-ZrPO and 30 wt%$WO_3$/M-ZrPO. Furthermore, the specific surface area, porosity and pore diameter of X wt%$WO_3$/M-ZrPO are summarized in Table 1. It could be observed that the specific surface area and pore volume decreased gradually with the increasing of $WO_3$ loading. This might be mainly due to that the loaded $WO_3$ species contributed little to the specific surface area and pore volume. Generally, all X wt%$WO_3$/M-ZrPO still preserved obvious mesostructure with large specific surface area, big pore volume and narrow pore size distribution even after a second high temperature calcination process, fully demonstrating the superior thermal stability of M-ZrPO. In

addition, the W atom density (atom·nm$^{-2}$) calculated from $WO_3$ loading and specific surface area is shown in Table 1. Combined with the WXRD and Raman analyses, it was concluded that the $WO_3$ species were highly dispersed on the M-ZrPO when the W atom density was below 4.30 atom·nm$^{-2}$ and crystalline $WO_3$ began to form at the W atom density of 5.95 atom·nm$^{-2}$. However, for 20 wt%$WO_3$/$ZrP_{sol\text{-}gel}$, the specific surface area only showed 24.9 $m^2 \cdot g^{-1}$ and the W atom density reached 20.9 atom·nm$^{-2}$. The high W atom density led to the formation of crystalline $WO_3$ in the surface of $ZrP_{sol\text{-}gel}$ and this conclusion also could be proved by WXRD pattern (as shown in Fig. S1). Therefore, M-ZrPO with high specific surface area was helpful for improving the dispersion of $WO_3$ species.

**Figure 5**

**Table 1**

### 3.2.3 TEM analysis

The morphology analysis of X wt%$WO_3$/M-ZrPO catalysts was characterized by TEM. The TEM images of all X wt%$WO_3$/M-ZrPO samples are shown in Fig. 6. Compared with the M-ZrPO carrier, the obvious mesopores also could be observed, indicating the mesostructure still existed in X wt%$WO_3$/M-ZrPO samples. This agreed quite well with the characterization of $N_2$-physisorption. Besides, it was interesting that no apparent $WO_3$ particles were observed in 25 wt%$WO_3$/M-ZrPO and 30 wt%$WO_3$/M-ZrPO, which had weak diffraction peaks of crystalline $WO_3$ in the WXRD patterns. This might be due to that the diffraction peaks were weak and

broad and the $WO_3$ existed as thin sheets with low crystallinity as reported by Yang *et al*.[52] Moreover, as shown in Fig. 6g , the exclusive Zr, P and W peaks could be clearly observed in the EDX pattern of 20 wt%$WO_3$/M-ZrPO, illustrating that the W species were successfully introduced into the materials.

**Figure 6**

### 3.2.4 UV-vis spectra analysis

The UV-vis spectra were utilized to distinguish the states of tungsten species in X wt%$WO_3$/M-ZrPO and shown in Fig. 7.[6,53] The support M-ZrPO showed an obvious absorption peak at 205 nm, which was attributed to the Zr-O-P coordination. An additional weak peak at about 300 nm could be ascribed to Zr (IV) interacting with the phosphate counter anions in the framework. As the introduction of $WO_3$, a new peak at 260 nm, which could be assigned to the low-condensed oligomeric tungsten species, could be discovered and became more observable with the increasing of $WO_3$ loading.[6,29] For the samples with $WO_3$ loading below 20 wt%, the absence of peaks at 400 nm indicated that no crystalline $WO_3$ existed in these samples and the tungsten species were highly dispersed on the surface of M-ZrPO. However, the weak band at 400 nm began to be observed for 25 wt%$WO_3$/M-ZrPO, implying that the crystalline $WO_3$ appeared in the sample. Further increasing the $WO_3$ content to 30 wt%, the intensity of band at 400 nm became stronger due to the increasing quantity of crystalline $WO_3$ species on the surface. In short, the tungsten species existed as low-condensed oligomeric states in the samples with $WO_3$ loading below 20 wt% and

crystalline $WO_3$ appeared in the 25 wt%$WO_3$/M-ZrPO and 30 wt%$WO_3$/M-ZrPO. The same conclusion also could be gotten from the WXRD and Raman characterizations.

**Figure 7**

### 3.2.5 FT-IR spectra analysis

The FT-IR spectra of X wt%$WO_3$/M-ZrPO are shown in Fig. 8. All the patterns of X wt%$WO_3$/M-ZrPO displayed obvious peaks at 3450 and 1630 $cm^{-1}$, which were assigned to the surface hydroxyl groups. The peak at 1070 $cm^{-1}$ was arised from the Zr-O-P network. Besides, a group of new peaks at 780, 630 and 470 $cm^{-1}$, which were characteristic of the stretching vibration mode of W-O-W,[32] appeared and were very weak in 5-20 wt%$WO_3$/M-ZrPO samples, in which the $WO_3$ species existed as low-condensed oligomeric states. Further increasing $WO_3$ loading content to 25 and 30 wt%, these peaks became more recognizable. We deduced this might be explained by the appearance of crystalline $WO_3$ in 25 wt%$WO_3$/M-ZrPO and 30 wt%$WO_3$/M-ZrPO. These conclusions agreed quite well with the WXRD, Raman and UV-vis characterizations.

**Figure 8**

### 3.2.6 $H_2$-TPR analysis

The $H_2$-TPR profiles of X wt%$WO_3$/M-ZrPO and bulk $WO_3$ are shown in Fig. 9. The M-ZrPO showed no discernible reduction peaks at 550-1100 $^oC$, whereas, the bulk $WO_3$ showed three main peaks at 790, 930 and 1000 $^oC$. These three peaks could

be assigned to the three-stepwise reduction of $WO_3$ to W ($WO_3$(VI) → $W_{20}O_{58}$(VI,V) → $WO_2$(IV) → W(0)).[54-55] However, the reduction of X wt%$WO_3$/M-ZrPO was strongly depended on the $WO_3$ loading. As reported in the literature, the reducibility of tungsten-based catalysts increased as the strength of interaction between metal oxide species and support decreased.[5,50,56] With the increasing of $WO_3$ loading from 5 to 30 wt%, a shift of reduction peaks to lower temperature was apparently observed, indicating that the interaction between $WO_3$ and support became weaker with the increasing of $WO_3$ loading. However, the reduction temperature was still much higher than bulk $WO_3$, illustrating the existence of intense interaction between $WO_3$ species and support. The strong interaction was in favor of reducing the sintering and leaching of tungsten species in the calcination and reaction process.[6]

**Figure 9**

### 3.2.7 XPS analysis

The high-resolution XPS analysis was employed to investigate the surface chemical composition as well as the oxidation state of tungsten species in X wt%$WO_3$/M-ZrPO. The W 4f XPS profiles of X wt%$WO_3$/M-ZrPO with different $WO_3$ loading are shown in Fig. 10(1). All XPS profiles in the W 4f region were similar to each other in shape and the intensity of W 4f region increased monotonously with the $WO_3$ loading. The core level spectra displayed two peaks corresponding to W $4f_{7/2}$ and W $4f_{5/2}$ with binding energies of 36.2 and 38.3 eV, which were related to the W(VI) oxidation state.[57] Therefore, it could be deduced that the tungsten species mainly existed as high

oxidation state W(VI) in the materials. The high oxidation state W(VI) might account for the improvement of Brønsted acidic property with the increasing of tungsten content in X wt%$WO_3$/M-ZrPO.

In addition, the correlation between surface $WO_3$ contents of gotten products calculated from XPS profiles and theoretical $WO_3$ contents as loaded in the preparation process is shown in Fig. 10(2). According to the comparison of surface $WO_3$ contents with theoretical values, it could be concluded that the $WO_3$ contents almost increased linearly with increasing of $WO_3$ loading. This might suggest that $WO_3$ species were dispersed uniformly on the surface of M-ZrPO even in the samples with high $WO_3$ loading (25 and 30 wt%).

**Figure 10**

### 3.2.8 Acidic property

The acidic property of X wt%$WO_3$/M-ZrPO was evaluated by $NH_3$-TPD. All the TPD profiles of X wt%$WO_3$/M-ZrPO are shown in Fig. 11. The characteristic TPD profile showed an obvious broad peak at 150-400 $^oC$. This indicated that abundant acid sites with different strength existed in X wt%$WO_3$/M-ZrPO. Furthermore, the desorption peaks of $NH_3$ at 200 $^oC$ became larger with the introduction of $WO_3$ and reached the maximum at 20 wt% $WO_3$ loading, indicating the acidity was improved with the introduction of tungsten species. Further increasing $WO_3$ loading to 25 and 30 wt%, the desorption peaks decreased, showing that the acidity began to decrease with the appearance of crystalline $WO_3$ in 25 wt%$WO_3$/M-ZrPO and 30

wt%$WO_3$/M-ZrPO. In addition, the peak at 320 $^oC$ which might be the Lewis acidity caused by Zr(IV), became weak with the increasing of tungsten loading. This might be due to the loaded $WO_3$ species covered on the surface of M-ZrPO and reduced the Lewis acid sites caused by the Zr(IV).

The pyridine-IR spectra recorded after adsorption of pyridine at room temperature and outgassed at 150 $^oC$ are shown in Fig. 12(1). The spectra showed bands at 1450, 1575 and 1610 $cm^{-1}$, ascribed to pyridine coordinately bonded to the Lewis acid sites. The samples showed bands at 1540 and 1640 $cm^{-1}$, which were due to protonated pyridine bonded to the Brønsted acid sites. The bands at 1490 $cm^{-1}$ were a combination between two separate bands at 1540 and 1450 $cm^{-1}$, indicating that both Brønsted and Lewis acid sites existed in the samples. When $WO_3$ loading increased from 0 to 20 wt%, the concentration of the Brønsted acid sites (bands at 1540 $cm^{-1}$) increased progressively. This might be owing to the increasing amounts of highly dispersed tungsten species on the surface of M-ZrPO. However, the amounts of Brønsted acid sites began to slightly decrease in 25 wt%$WO_3$/M-ZrPO and 30 wt%$WO_3$/M-ZrPO, possibly due to that the high content of $WO_3$ led to appearance of crystalline $WO_3$ in the two samples. Moreover, the spectra of X wt%$WO_3$/M-ZrPO outgassed at 250 $^oC$ are shown in Fig. 12(2). In the spectra, the band at 1540 $cm^{-1}$ disappeared in the sample without introduction of $WO_3$. However, the spectra of 20 wt%$WO_3$/M-ZrPO still showed observable band at 1540 $cm^{-1}$, illustrating that Brønsted acidity caused by the loaded tungsten species in 20 wt%$WO_3$/M-ZrPO was rather stronger than the Brønsted acidity in M-ZrPO. The Brønsted acid sites in 20

wt%$WO_3$/M-ZrPO gradually vanished with the desorption temperature reached 300 and 400 $^oC$ (as shown in Fig. S2). Moreover, the Brønsted and Lewis acidity gotten from pyridine-IR spectra outgassed at 150 $^oC$ is shown in Table 2. The Brønsted acidity increased gradually and reached the maximum at 20 wt% $WO_3$ loading for 43.4 $\mu mol \cdot g^{-1}$. Further increasing $WO_3$ loading to 25 and 30 wt%, the Brønsted acidity began to decrease gradually. We deduced that the $WO_3$ dispersion state on surface of support could largely affect the Brønsted acidic properties. When the tungsten species were highly dispersed on support ($WO_3$ loading $\leq$20 wt%), the surface Brønsted acidity increased with the increasing of $WO_3$ loading. The loaded $WO_3$ species could be probably responsible for enhancing Brønsted acidity. Beyond the monolayer coverage, due to agglomeration of tungsten species and formation of crystalline $WO_3$ (as proved from XRD, Raman and UV-vis analyses), gradual loss of Brønsted acidity was observed in 25 wt%$WO_3$/M-ZrPO and 30 wt%$WO_3$/M-ZrPO (as shown in Scheme 1).[49] The strong Brønsted acid sites were essential to the benzylation of anisole with benzyl alcohol.

**Figure 11**

**Figure 12**

**Scheme 1**

**Table 2**

### 3.3 Catalytic performance

The catalytic performance of X wt%$WO_3$/M-ZrPO was investigated in liquid phase

benzylation of anisole with benzyl alcohol. All the reaction schemes are presented in Scheme 2. In this reaction system, benzylanisoles are the products of benzylation of anisole with benzyl alcohol and dibenzyl ether is a product of the auto-etherification of benzyl alcohol. Meanwhile, dibenzyl ether also can react with anisole to produce benzylanisole.

To investigate the influence of $WO_3$ loading on catalytic activity, the catalytic performance of X wt%$WO_3$/M-ZrPO with different $WO_3$ loading was investigated in benzylation reaction and the results are shown in Fig. 13(1). As shown in Fig. 13(1), the sample without supporting $WO_3$ showed poor catalytic activity for benzylation reaction, and only showed 18.0% conversion of benzyl alcohol with 54.5% selectivity of benzylanisoles. However, with introduction of tungsten species, both the conversion and selectivity were largely improved and reached 76.3% and 74.8% at 5 wt% $WO_3$ loading. Further increase $WO_3$ loading, the conversion and selectivity were stepwise improved and reached the maximum at 20 wt% $WO_3$ loading with the 100% conversion of benzyl alcohol and 91.0% selectivity of benzylanisole. Therefore, the loaded $WO_3$ species successfully improved the catalytic activity of X wt%$WO_3$/M-ZrPO in benzylation reaction. In the literature, there is a general agreement that the benzylation of anisole with benzyl alcohol is catalyzed on the Brønsted acid sites.[58-59] Therefore, the improved catalytic activity might be due to the increasing of Brønsted acid sites with increasing of $WO_3$ loading. However, for 25 wt%$WO_3$/M-ZrPO and 30 wt%$WO_3$/M-ZrPO, the catalytic activity began to fall gradually. This might be on account of the active sites were covered by crystalline

$WO_3$ and the number of Brønsted acidic sites decreased for excess $WO_3$ loading. Based on the characterization results presented above, it could be concluded that the proper content of tungsten oxide species and its highly dispersed state have a significant effect on the catalytic performance of X wt%$WO_3$/M-ZrPO solid acid catalysts. The samples with highly dispersed tungsten oxide species showed high conversion and selectivity for the benzylation reaction, whereas the appearance of $WO_3$ crystallites decreased the catalytic performance of X wt%$WO_3$/M-ZrPO.

The changing progress of benzyl alcohol conversion and benzylanisole yield was studied by analyzing the reaction products at different time intervals (Fig. 13(2)). Initially, the conversion of benzyl alcohol and yield of benzylanisole increased with time and the maximum benzyl alcohol conversion (100%) and benzylanisole yield (91.0%) were achieved at 120 min for 20 wt%$WO_3$/M-ZrPO. After 120 min, there were little changes in the curves. Moreover, when solid acid catalyst was employed, a crucial issue was possibility that the active sites might migrate from solid support to liquid phase and these leached species might become responsible for a significant part of the catalytic activity.[42,60] In order to determine if the tungsten species leaching from support, we investigated the yield of benzylanisoles with and without filtering 20 wt%$WO_3$/M-ZrPO solid acid catalyst. As shown in Fig. 13(2), the liquid phase was separated from the reaction system at 40 min. No further reaction was observed after filtering the solid acid catalyst, proving that the benzylation reaction was only being possible in the presence of 20 wt%$WO_3$/M-ZrPO solid acid catalyst and 20 wt%$WO_3$/M-ZrPO was a real heterogeneous catalyst. In addition, the possible

leaching of $WO_3$ species into the reaction mixture was determined by the atomic adsorption spectroscopy (AAS) analysis. No detectable tungsten species could be found in the mixture, indicating that no obvious tungsten species leached to the mixture in the reaction process.

**Figure 13**

**Scheme 2**

Moreover, in solid acid catalyzed reactions, both high activity and reusability are significant in consideration of the separation of products and recycling of the catalyst. In order to check the recyclability of the catalyst, we carried out five runs test over 20 wt%$WO_3$/M-ZrPO (shown in Fig. 14(1)). Compared with the fresh catalyst, no significant declines in conversion and selectivity were observed after five cycles, indicating that 20 wt%$WO_3$/M-ZrPO could be reused as solid acid catalyst in the benzylation reaction. Moreover, to investigate the stability and persistence of active tungsten species, 20 wt%$WO_3$/M-ZrPO catalyst recovered after five cycles was characterized by XPS analysis and the results showed that surface $WO_3$ content (20.6 wt%) changed little compared with fresh sample (20.1 wt%). All these results might be due to the presence of strong interaction between active tungsten species and M-ZrPO and the leaching of tungsten species were largely avoided in the reaction process. In addition, the catalyst regenerated after five cycles was characterized by $N_2$-physisorption and TEM. As shown in Fig. S3 and S4, the mesostructure of 20 wt%$WO_3$/M-ZrPO still existed and the textural properties (shown in Table 1) of used

catalyst changed little, indicating that the catalyst suffered little damage in the acid-catalyzed reaction. Moreover, Fig. 14(2) showed the activity of 20 wt%$WO_3$/M-ZrPO and control catalysts (H-Beta, H-ZSM5 and 20 wt%$WO_3$/$ZrP_{sol\text{-}gel}$) in the benzylation reaction. Compared with the control catalysts, 20 wt%$WO_3$/M-ZrPO showed a markedly higher catalytic activity. It was noteworthy that 20 wt%$WO_3$/$ZrP_{sol\text{-}gel}$ only showed 41.7% conversion of benzyl alcohol with 76.9% selectivity of benzylanisoles. This might be due to that the poor dispersion of tungsten species on the $ZrP_{sol\text{-}gel}$ and crystalline $WO_3$ appeared at a 20 wt% loading leaded to weak Brønsted acidity (as shown in Table 2). Therefore, the mesoporous structure was propitious for improving the dispersion of tungsten species on support to provide more additional active sites for the reactant molecules resulting in improved catalytic performance. Therefore, 20 wt%$WO_3$/M-ZrPO was an ideal solid acid catalyst in benzylation reaction due to the excellent catalytic activity and recyclability.

**Figure 14**

## 4. Conclusion

A series of $WO_3$ supported on ordered mesoporous zirconium oxophosphate (X wt%$WO_3$/M-ZrPO) solid acid catalysts with different $WO_3$ loading from 5 to 30 wt% were successfully synthesized and showed excellent catalytic performance in benzylation of anisole. Moreover, compared with traditional zirconium phosphate synthesized from sol-gel method ($ZrP_{sol\text{-}gel}$), the M-ZrPO with abundant ordered

mesostructure was a better candidate to obtain highly dispersed tungsten species in the samples. The state of $WO_3$ largely influenced the catalytic performance of X wt%$WO_3$/M-ZrPO. When $WO_3$ species existed as highly dispersed state (≤ 20 wt%), the Brønsted acidic properties and catalytic performance was improved with the increasing of $WO_3$ loading. However, the Brønsted acidic properties and catalytic performance began to decrease with the formation of crystalline $WO_3$ (≥ 25 wt%). Moreover, due to the strong interaction between $WO_3$ and M-ZrPO, both sintering and leaching of tungsten species could be greatly restrained. Therefore, the X wt%$WO_3$/M-ZrPO catalysts showed excellent stability and reusability in the benzylation of anisole.

**Acknowledgements**

The authors sincerely acknowledge the financial support from the National Basic Research Program of PR China (No. 2011CB201404) and the National Natural Science Foundation of China (No. 21133011).

**Notes and references**

[a] State Key Laboratory for Oxo Synthesis and Selective Oxidation, Lanzhou Institute of Chemical Physics, Chinese Academy of Sciences, Lanzhou 730000, People's Republic of China.

[b] University of Chinese Academy of Sciences, Beijing 100049, People's Republic of China.

[c] Suzhou Institute of Nano-Tech and Nano-Bionics, Chinese Academy of Sciences, Suzhou 215123, People's Republic of China.

[*] Corresponding author: e-mail: **ljchou@licp.cas.cn** (L. J. Chou), Tel: +86 0931 4968066; Fax: +86 0931 4968129

Electronic Supplementary Information (ESI) available: The Wide-angle X-ray diffraction of 20 wt%$WO_3$/$ZrP_{sol\text{-}gel}$, IR spectra for pyridine adsorbed on the 20 wt%$WO_3$/M-ZrPO recorded at different temperatures, isotherms and pore size distribution and TEM images of 20 wt%$WO_3$/M-ZrPO-used after five cycles.

1. M. Hino and K. Arata, *J. Chem. Soc., Chem. Commun.*, 1988, 1259-1260.
2. R. D. Wilson, D. G. Barton, C. D. Baertsch and E. Iglesia, *J. Catal.*, 2000, **194**, 175-187.
3. Y. Rezgui and M. Guemini, *Appl. Catal., A.*, 2005, **282**, 45-53.
4. Y. Rezgui and M. Guemini, *Energ. Fuel*, 2007, **21**, 602-609.
5. A. de Lucas, J. L. Valverde, P. Cañizares and L. Rodriguez, *Appl. Catal., A.*, 1998, **172**, 165-176.
6. X. L. Yang, W. L. Dai, R. Gao and K. Fan, *J. Catal.*, 2007, **249**, 278-288.
7. C. Hammond, J. Straus, M. Righettoni, S. E. Pratsinis and I. Hermans, *ACS Catal.*, 2013, **3**, 321-327.
8. H. Kamata, K. Takahashi and C. U. Ingemar Odenbrand, *J. Catal.*, 1999, **185**, 106-113.
9. W. Shan, F. Liu, H. He, X. Shi and C. Zhang, *Appl. Catal., B.*, 2012, **115–116**,

100-106.

10. F. Can, S. Berland, S. Royer, X. Courtois and D. Duprez, *ACS Catal.*, 2013, **3**, 1120-1132.

11. C. Liu, L. Chen, H. Chang, L. Ma, Y. Peng, H. Arandiyan and J. Li, *Catal. Commun.*, 2013, **40**, 145-148.

12. T. Kabe, W. Qian, A. Funato, Y. Okoshi and A. Ishihara, *Phys. Chem. Chem. Phys.*, 1999, **1**, 921-927.

13. A. Wang, X. Li, Y. Chen, D. Han, Y. Wang, Y. Hu and T. Kabe, *Chem. Lett.*, 2001, **30**, 474-475.

14. L. Coulier, G. Kishan, J. A. R. van Veen and J. W. Niemantsverdriet, *J. Phys. Chem. B*, 2002, **106**, 5897-5906.

15. S. D. Kelly, N. Yang, G. E. Mickelson, N. Greenlay, E. Karapetrova, W. Sinkler and S. R. Bare, *J. Catal.*, 2009, **263**, 16-33.

16. D. Barton, S. Soled and E. Iglesia, *Top. Catal.*, 1998, **6**, 87-99.

17. W. Zhou, E. I. Ross-Medgaarden, W. V. Knowles, M. S. Wong, I. E. Wachs and C. J. Kiely, *Nat Chem*, 2009, **1**, 722-728.

18. N. Soultanidis, W. Zhou, A. C. Psarras, A. J. Gonzalez, E. F. Iliopoulou, C. J. Kiely, I. E. Wachs and M. S. Wong, *J. Am. Chem. Soc.*, 2010, **132**, 13462-13471.

19. N. Mizuno and M. Misono, *Chem. Rev.*, 1998, **98**, 199-218.

20. K. Tanabe and W. F. Hölderich, *Appl. Catal., A.*, 1999, **181**, 399-434.

21. V. M. Benitez and N. S. Fígoli, *Catal. Commun.*, 2002, **3**, 487-492.

22. X. Chen, G. Clet, K. Thomas and M. Houalla, *J. Catal.*, 2010, **273**, 236-244.

23. G. Lu, X. Li, Z. Qu, Q. Zhao, H. Li, Y. Shen and G. Chen, *Chem. Eng. J.*, 2010, **159**, 242-246.

24. J. E. Herrera, J. H. Kwak, J. Z. Hu, Y. Wang, C. H. F. Peden, J. Macht and E. Iglesia, *J. Catal.*, 2006, **239**, 200-211.

25. C. D. Baertsch, K. T. Komala, Y.-H. Chua and E. Iglesia, *J. Catal.*, 2002, **205**, 44-57.

26. N. R. Shiju, M. AnilKumar, W. F. Hoelderich and D. R. Brown, *J. Phys. Chem. C*, 2009, **113**, 7735-7742.

27. R. Kourieh, S. Bennici, M. Marzo, A. Gervasini and A. Auroux, *Catal. Commun.*, 2012, **19**, 119-126.

28. S. Furuta, H. Matsuhashi and K. Arata, *Catal. Commun.*, 2004, **5**, 721-723.

29. K. N. Rao, A. Sridhar, A. F. Lee, S. J. Tavener, N. A. Young and K. Wilson, *Green Chem.*, 2006, **8**, 790-797.

30. M. K. Lam and K. T. Lee, *Fuel Process. Technol.*, 2011, **92**, 1639-1645.

31. G. Chandra Behera and K. M. Parida, *Dalton. Trans.*, 2012, **41**, 1325-1331.

32. W. Xie and D. Yang, *Bioresource Technol.*, 2012, **119**, 60-65.

33. J. S. Beck, J. C. Vartuli, W. J. Roth, M. E. Leonowicz, C. T. Kresge, K. D. Schmitt, C. T. W. Chu, D. H. Olson and E. W. Sheppard, *J. Am. Chem. Soc.*, 1992, **114**, 10834-10843.

34. C. T. Kresge, M. E. Leonowicz, W. J. Roth, J. C. Vartuli and J. S. Beck, *Nature*, 1992, **359**, 710-712.

35. Y. Rao, M. Trudeau and D. Antonelli, *J. Am. Chem. Soc.*, 2006, **128**, 13996-13997.

36. J. Fan, Y. Dai, Y. Li, N. Zheng, J. Guo, X. Yan and G. D. Stucky, *J. Am. Chem. Soc.*, 2009, **131**, 15568-15569.

37. Q. Yuan, A. X. Yin, C. Luo, L. D. Sun, Y. W. Zhang, W. T. Duan, H. C. Liu and C. H. Yan, *J. Am. Chem. Soc.*, 2008, **130**, 3465-3472.

38. L. Xu, H. Zhao, H. Song and L. Chou, *Int. J. Hydrogen. Energ*, 2012, **37**, 7497-7511.

39. A. Bordoloi and S. B. Halligudi, *J. Catal.*, 2008, **257**, 283-290.

40. D. Hua, S. L. Chen, G. Yuan, Y. Wang, Q. Zhao, X. Wang and B. Fu, *Micropor. Mesopor. Mater.*, 2011, **143**, 320-325.

41. G. A. Olah, *Friedel-Crafts Chemistry*, Wiley, New York, 1973.

42. F. Wang and W. Ueda, *Chem. Eur. J.*, 2009, **15**, 742-753.

43. J. Dou and H. C. Zeng, *J. Am. Chem. Soc.*, 2012, **134**, 16235-16246.

44. C. R. Kumar, K. Jagadeeswaraiah, P. S. S. Prasad and N. Lingaiah, *ChemCatChem*, 2012, **4**, 1360-1367.

45. Z. Miao, L. Xu, H. Song, H. Zhao and L. Chou, *Catal. Sci. Technol.*, 2013, **3**, 1942-1954.

46. F. A. H. Al-Qallaf, L. F. Hodson, R. A. W. Johnstone, J. Y. Liu, L. Lu and D. Whittaker, *J. Mol. Catal. A: Chem.*, 2000, **152**, 187-200.

47. A. S. Khder and A. I. Ahmed, *Appl. Catal., A.*, 2009, **354**, 153-160.

48. C. A. Emeis, *J. Catal.*, 1993, **141**, 347-354.

49. D. G. Barton, M. Shtein, R. D. Wilson, S. L. Soled and E. Iglesia, *J. Phys. Chem. B*, 1999, **103**, 630-640.

50. A. Martínez, G. Prieto, M. A. Arribas, P. Concepción and J. F. Sánchez-Royo, *J. Catal.*, 2007, **248**, 288-302.

51. K. Song, H. Zhang, Y. Zhang, Y. Tang and K. Tang, *J. Catal.*, 2013, **299**, 119-128.

52. X. L. Yang, R. Gao, W. L. Dai and K. Fan, *J. Phys. Chem. C*, 2008, **112**, 3819-3826.

53. M. S. Morey, J. D. Bryan, S. Schwarz and G. D. Stucky, *Chem. Mater.*, 2000, **12**, 3435-3444.

54. D. C. Vermaire and P. C. van Berge, *J. Catal.*, 1989, **116**, 309-317.

55. D. G. Barton, S. L. Soled, G. D. Meitzner, G. A. Fuentes and E. Iglesia, *J. Catal.*, 1999, **181**, 57-72.

56. A. Ramanathan, R. Maheswari, B. P. Grady, D. S. Moore, D. H. Barich and B. Subramaniam, *Micropor. Mesopor. Mater.*, 2013, **175**, 43-49.

57. F. Di Gregorio and V. Keller, *J. Catal.*, 2004, **225**, 45-55.

58. M. H. C. de la Cruz, M. A. Abdel-Rehim, A. S. Rocha, J. F. C. da Silva, A. da Costa Faro Jr and E. R. Lachter, *Catal. Commun.*, 2007, **8**, 1650-1654.

59. T. Kitano, T. Shishido, K. Teramura and T. Tanaka, *J. Phys. Chem. C*, 2012, **116**, 11615-11625.

60. N. T. S. Phan, K. K. A. Le and T. D. Phan, *Appl. Catal., A.*, 2010, **382**, 246-253.

**Table 1.** Textural properties of the X wt%$WO_3$/M-ZrPO, 20 wt%$WO_3$/ $ZrP_{sol\text{-}gel}$ and 20 wt%$WO_3$/M-ZrPO-used derived from nitrogen adsorption and desorption data

| Sample | $WO_3$ loading | Specific Surface Area ($m^2 \cdot g^{-1}$) | Pore size (nm) | Pore Volume ($cm^3 \cdot g^{-1}$) | W atom density ($atom \cdot nm^{-2}$) |
|---|---|---|---|---|---|
| M-ZrPO | 0 | 165.5 | 5.63 | 0.25 | 0 |
| 5 wt%$WO_3$/M-ZrPO | 5 | 157.2 | 5.61 | 0.21 | 0.83 |
| 10 wt%$WO_3$/M-ZrPO | 10 | 151.1 | 5.63 | 0.21 | 1.72 |
| 15 wt%$WO_3$/M-ZrPO | 15 | 128.8 | 5.62 | 0.19 | 3.03 |
| 20 wt%$WO_3$/M-ZrPO | 20 | 120.8 | 5.64 | 0.18 | 4.30 |
| 25 wt%$WO_3$/M-ZrPO | 25 | 109.1 | 5.65 | 0.17 | 5.95 |
| 30 wt%$WO_3$/M-ZrPO | 30 | 96.5 | 5.70 | 0.15 | 8.08 |
| 20 wt%$WO_3$/ $ZrP_{sol\text{-}gel}$ | 20 | 24.9 | — | — | 20.9 |
| 20 wt%$WO_3$/M-ZrPO-used | 20 | 110.5 | 5.62 | 0.17 | 4.70 |

**Table 2.** The acidity of X wt%$WO_3$/M-ZrPO gotten from Pyridine-IR outgassed at 150 $^oC$

| Samples | Brønsted acidity ($\mu mol \cdot g^{-1}$) | Lewis acidity ($\mu mol \cdot g^{-1}$) | Total acidity ($\mu mol \cdot g^{-1}$) |
|---|---|---|---|
| M-ZrPO | 20.0 | 83.0 | 103.0 |
| 5 wt%$WO_3$/M-ZrPO | 33.9 | 80.0 | 113.9 |
| 10 wt%$WO_3$/M-ZrPO | 40.2 | 88.5 | 128.7 |
| 15 wt%$WO_3$/M-ZrPO | 42.2 | 77.4 | 119.6 |
| 20 wt%$WO_3$/M-ZrPO | 43.4 | 84.3 | 127.7 |
| 25 wt%$WO_3$/M-ZrPO | 30.0 | 66.5 | 96.5 |
| 30 wt%$WO_3$/M-ZrPO | 25.0 | 63.0 | 88.0 |
| 20 wt%$WO_3$/$ZrP_{sol\text{-}gel}$ | 9.70 | 41.3 | 51.0 |

**Figure captions:**

**Figure 1.** Small-angle X-ray diffraction pattern **(1)** and Wide-angle X-ray diffraction pattern **(inset of (1))**, isotherms **(2)** and pore size distribution **(inset of (2))** of the support M-ZrPO.

**Figure 2.** TEM images of the M-ZrPO.

**Figure 3.** Wide-angle X-ray diffraction patterns of X wt%$WO_3$/M-ZrPO: **(a)** 5 wt%$WO_3$/M-ZrPO, **(b)** 10 wt%$WO_3$/M-ZrPO, **(c)** 15 wt%$WO_3$/M-ZrPO, **(d)** 20 wt%$WO_3$/M-ZrPO, **(e)** 25 wt%$WO_3$/M-ZrPO, **(f)** 30 wt%$WO_3$/M-ZrPO.

**Figure 4.** Raman spectra of the X wt%$WO_3$/M-ZrPO and bulk $WO_3$: **(a)** M-ZrPO, **(b)** 5 wt%$WO_3$/M-ZrPO, **(c)** 10 wt%$WO_3$/M-ZrPO, **(d)** 15 wt%$WO_3$/M-ZrPO, **(e)** 20 wt%$WO_3$/M-ZrPO, **(f)** 25 wt%$WO_3$/M-ZrPO, **(g)** 30 wt%$WO_3$/M-ZrPO, **(h)** bulk $WO_3$.

**Figure 5.** Isotherms **(1)** and pore size distributions **(2)** of the X wt%$WO_3$/M-ZrPO: **(a)** 5 wt%$WO_3$/M-ZrPO, **(b)** 10 wt%$WO_3$/M-ZrPO, **(c)** 15 wt%$WO_3$/M-ZrPO, **(d)** 20 wt%$WO_3$/M-ZrPO, **(e)** 25 wt%$WO_3$/M-ZrPO, **(f)** 30 wt%$WO_3$/M-ZrPO.

**Figure 6.** TEM images of the X wt%$WO_3$/M-ZrPO: **(a)** 5 wt%$WO_3$/M-ZrPO, **(b)** 10 wt%$WO_3$/M-ZrPO, **(c)** 15 wt%$WO_3$/M-ZrPO, **(d)** 20 wt%$WO_3$/M-ZrPO, **(e)** 25 wt%$WO_3$/M-ZrPO, **(f)** 30 wt%$WO_3$/M-ZrPO, **(g)** EDX measurement of 20 wt%$WO_3$/M-ZrPO. (The scale in images **(a-f)** was 50 nm)

**Figure 7.** UV-vis diffuse reflectance spectra of the X wt%$WO_3$/M-ZrPO: **(a)** M-ZrPO, **(b)** 5 wt%$WO_3$/M-ZrPO, **(c)** 10 wt%$WO_3$/M-ZrPO, **(d)** 15 wt%$WO_3$/M-ZrPO, **(e)** 20 wt%$WO_3$/M-ZrPO, **(f)** 25 wt%$WO_3$/M-ZrPO, **(g)** 30 wt%$WO_3$/M-ZrPO.

**Figure 8.** FT-IR spectra of the X wt%$WO_3$/M-ZrPO: **(a)** M-ZrPO, **(b)** 5 wt%$WO_3$/M-ZrPO, **(c)** 10 wt%$WO_3$/M-ZrPO, **(d)** 15 wt%$WO_3$/M-ZrPO, **(e)** 20 wt%$WO_3$/M-ZrPO, **(f)** 25 wt%$WO_3$/M-ZrPO, **(g)** 30 wt%$WO_3$/M-ZrPO.

**Figure 9.** The $H_2$-TPR profiles of the X wt%$WO_3$/M-ZrPO: **(a)** M-ZrPO, **(b)** 5 wt%$WO_3$/M-ZrPO, **(c)** 10 wt%$WO_3$/M-ZrPO, **(d)** 15 wt%$WO_3$/M-ZrPO, **(e)** 20 wt%$WO_3$/M-ZrPO, **(f)** 25 wt%$WO_3$/M-ZrPO, **(g)** 30 wt%$WO_3$/M-ZrPO, **(h)** bulk $WO_3$.

**Figure 10. (1)** High-resolution XPS spectra of the X wt%$WO_3$/M-ZrPO: **(a)** 5 wt%$WO_3$/M-ZrPO, **(b)** 10 wt%$WO_3$/M-ZrPO, **(c)** 15 wt%$WO_3$/M-ZrPO, **(d)** 20 wt%$WO_3$/M-ZrPO, **(e)** 25 wt%$WO_3$/M-ZrPO, **(f)** 30 wt%$WO_3$/M-ZrPO; **(2)** the realtion between $WO_3$ loading and $WO_3$ content calculated from XPS spectra.

**Figure 11.** $NH_3$-TPD profiles of the X wt%$WO_3$/M-ZrPO: **(a)** M-ZrPO, **(b)** 5 wt%$WO_3$/M-ZrPO, **(c)** 10 wt%$WO_3$/M-ZrPO, **(d)** 15 wt%$WO_3$/M-ZrPO, **(e)** 20 wt%$WO_3$/M-ZrPO, **(f)** 25 wt%$WO_3$/M-ZrPO, **(g)** 30 wt%$WO_3$/M-ZrPO.

**Figure 12.** IR spectra for pyridine adsorbed on the X wt%$WO_3$/M-ZrPO recorded at 150 $^{o}$C **(1)** and 250 $^{o}$C **(2)**: **(a)** M-ZrPO, **(b)** 5 wt%$WO_3$/M-ZrPO, **(c)** 10 wt%$WO_3$/M-ZrPO, **(d)** 15 wt%$WO_3$/M-ZrPO, **(e)** 20 wt%$WO_3$/M-ZrPO, **(f)** 25 wt%$WO_3$/M-ZrPO, **(g)** 30 wt%$WO_3$/M-ZrPO.

**Figure 13.** Friedel-Crafts benzylation reaction: **(1)** catalyzed by X wt%$WO_3$/M-ZrPO with different $WO_3$ loading; **(2)** catalyzed by 20 wt%$WO_3$/M-ZrPO at different times (BA: benzylanisoles).

**Figure 14.** Friedel-Crafts benzylation reaction: **(1)** the recyclability of 20

wt%$WO_3$/M-ZrPO; **(2)** catalyzed by different solid acid catalysts.

**Scheme 1.** The $WO_3$ state on the X wt%$WO_3$/M-ZrPO with increasing of $WO_3$ loading.

**Scheme 2.** Friedel-Crafts benzylation reaction between anisole and benzyl alcohol.

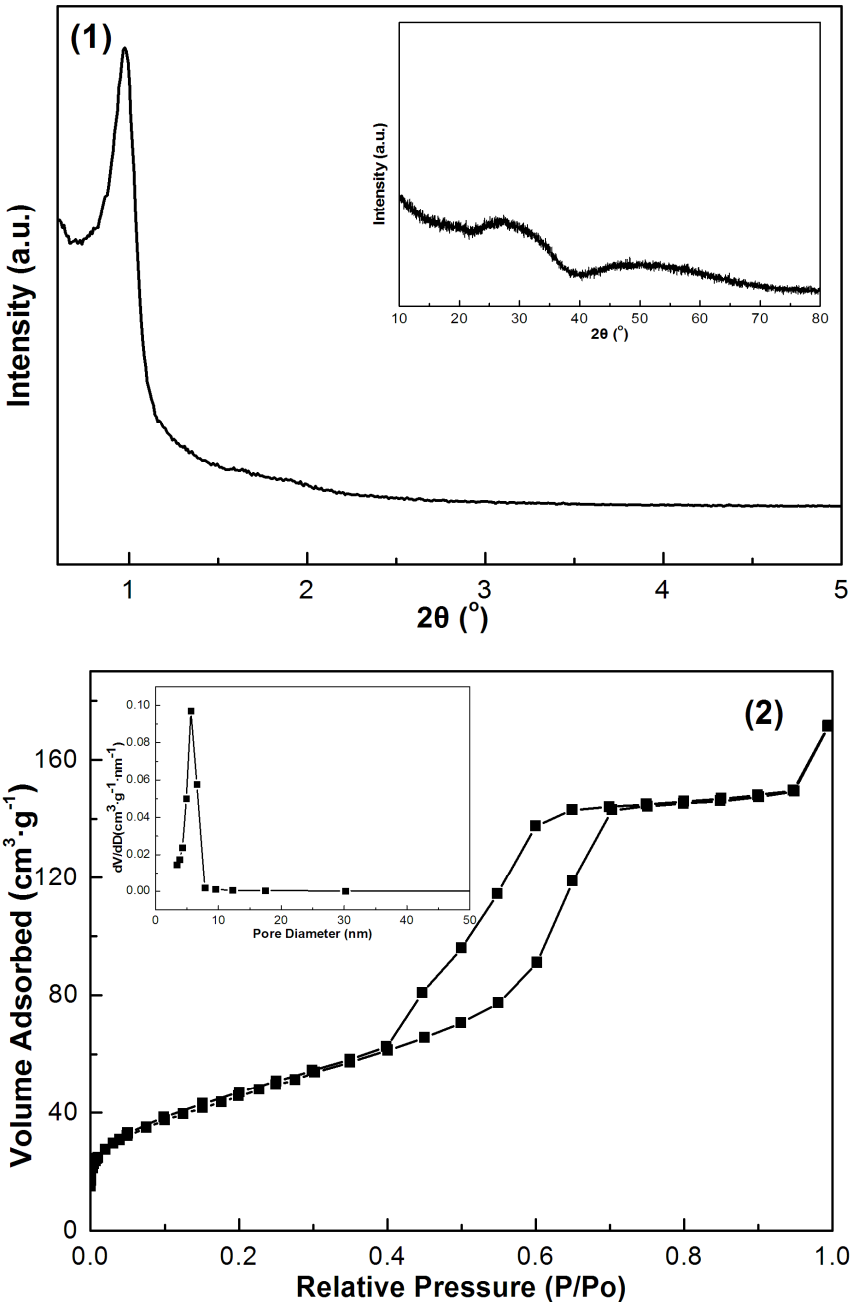


**Figure 1**

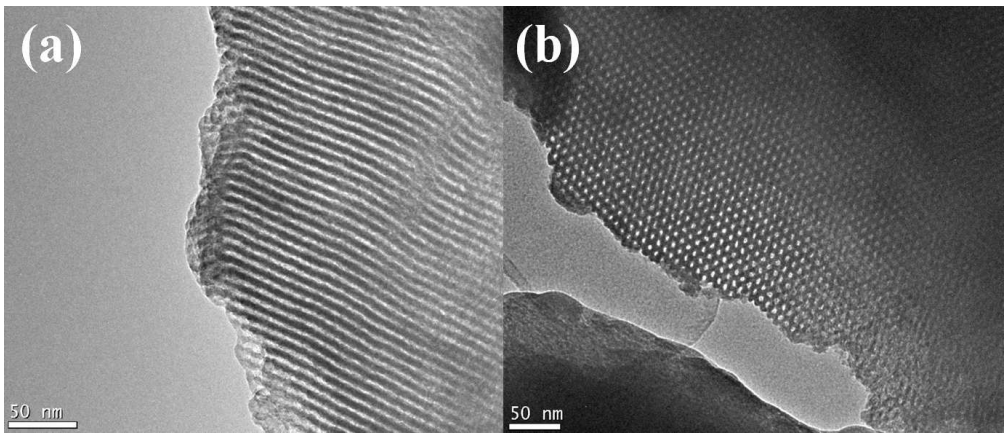


**Figure 2**

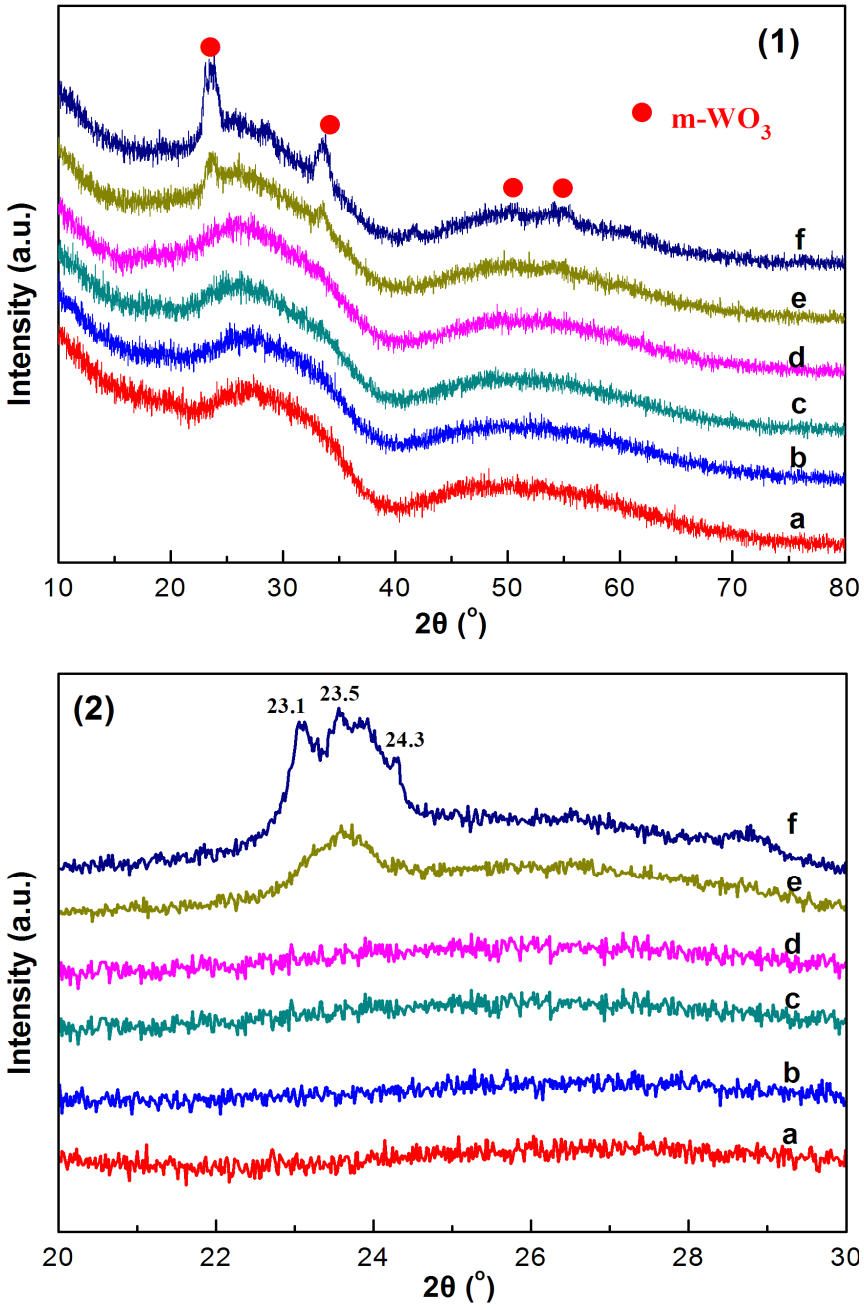


Figure 3

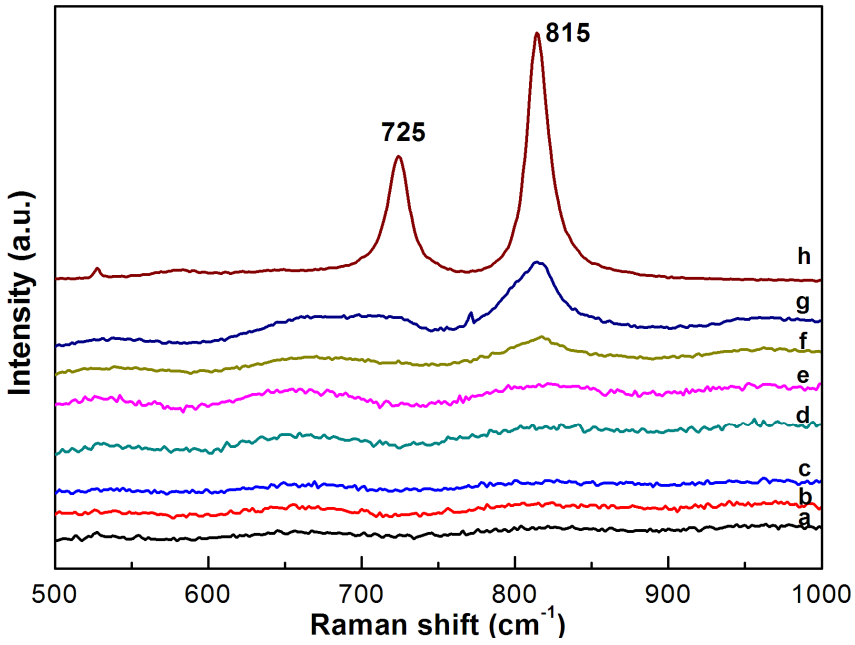


**Figure 4**

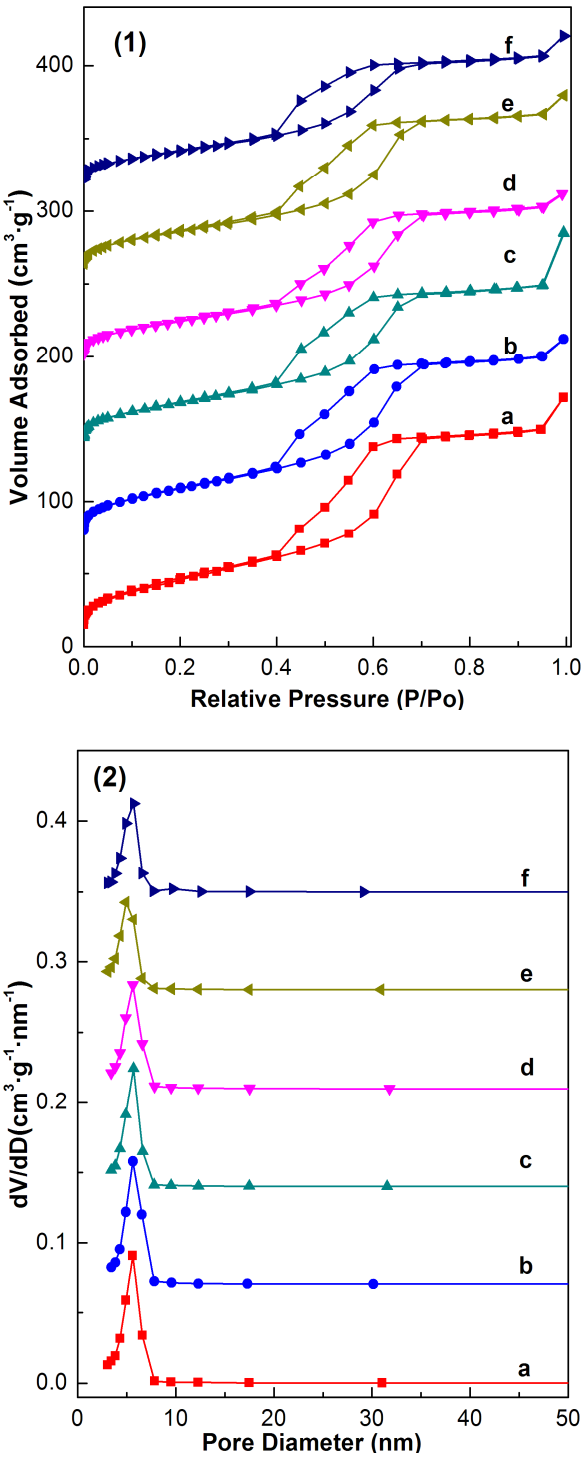


Figure 5

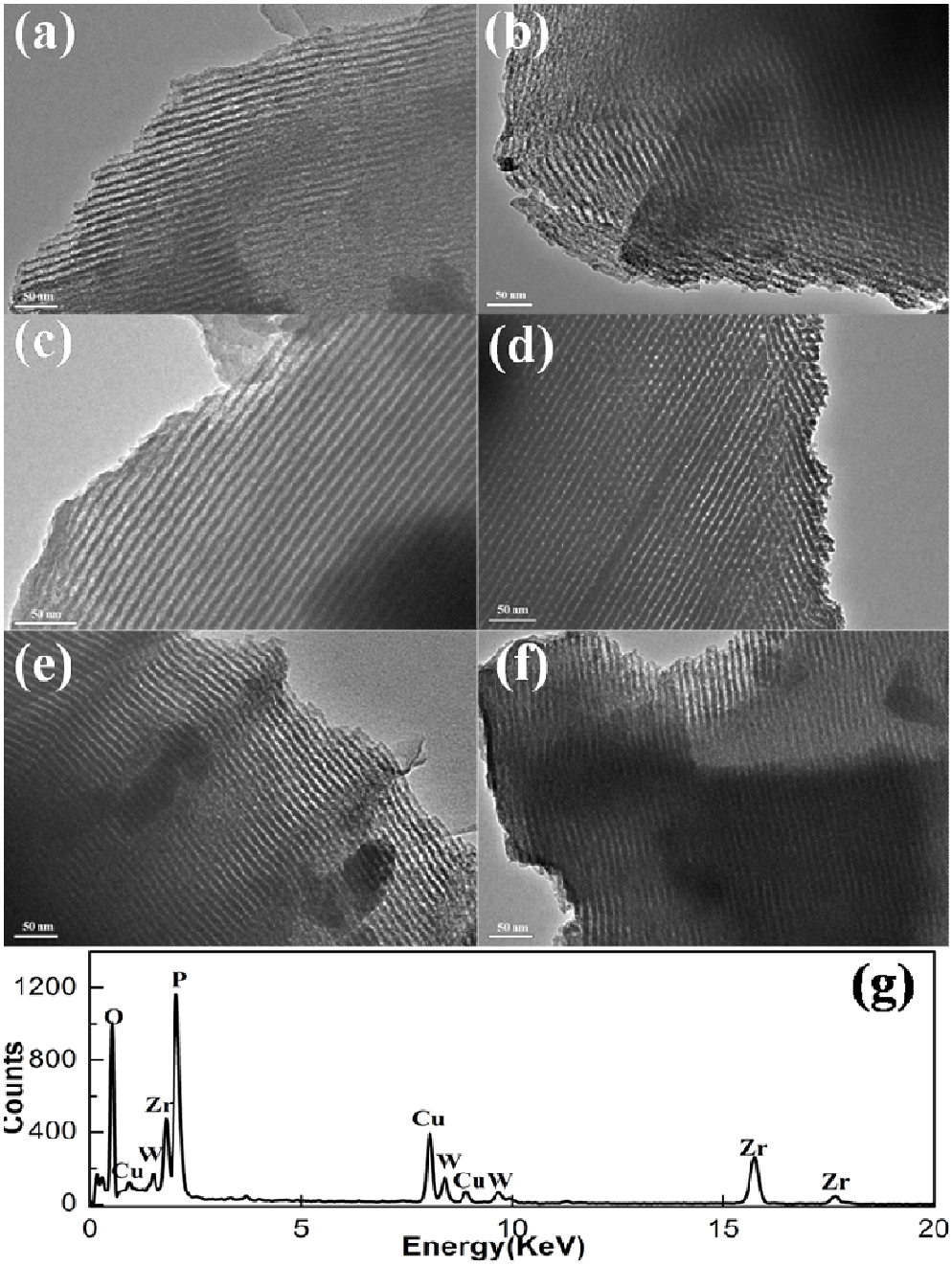


**Figure 6**

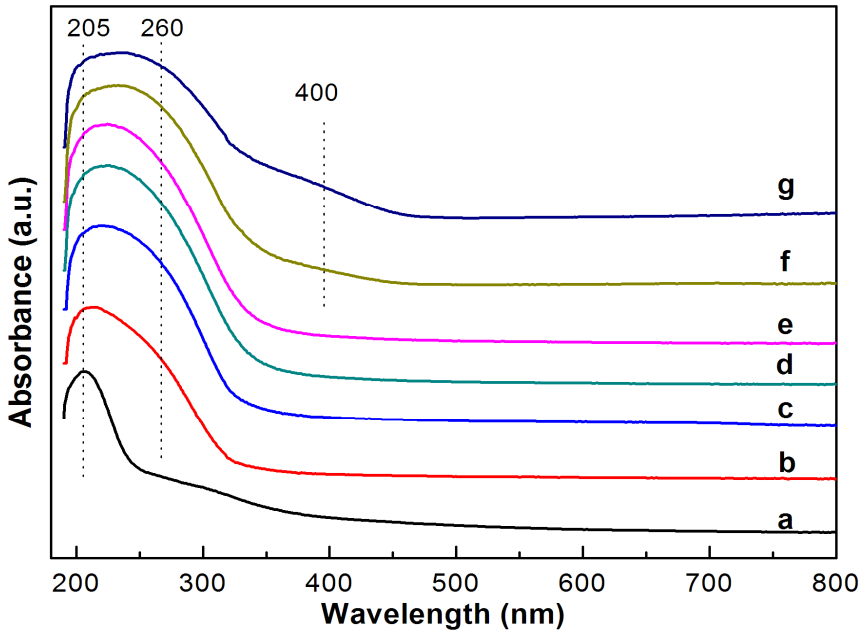


**Figure 7**

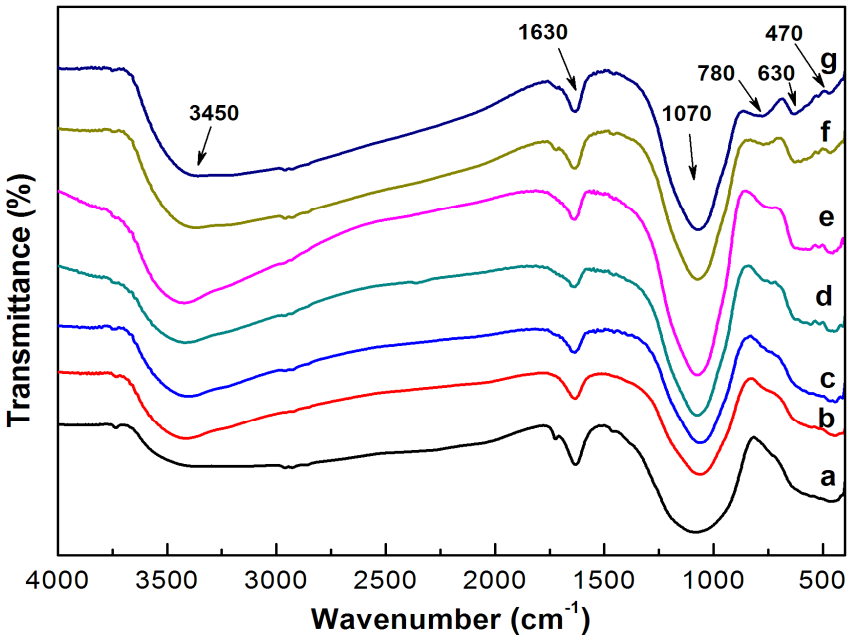


**Figure 8**

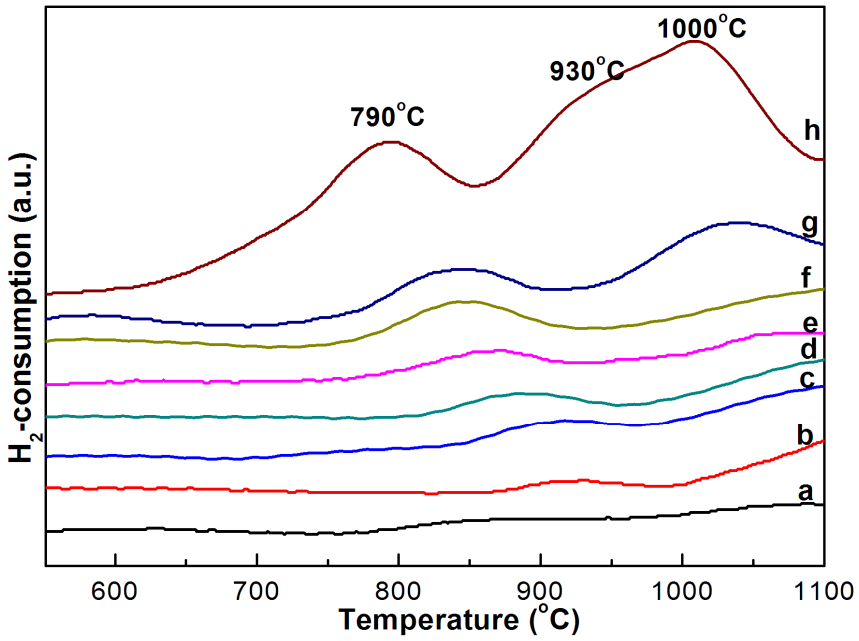


**Figure 9**

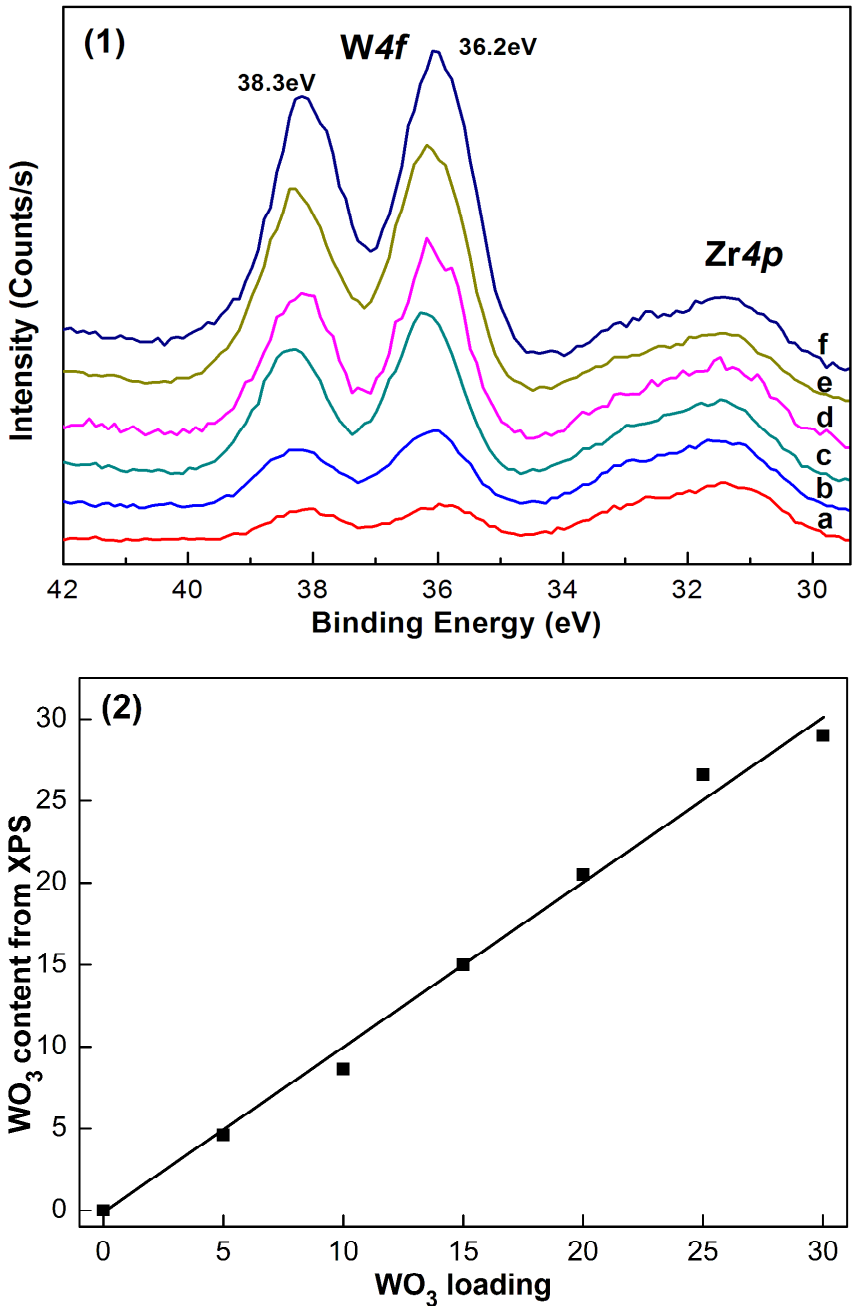


Figure 10

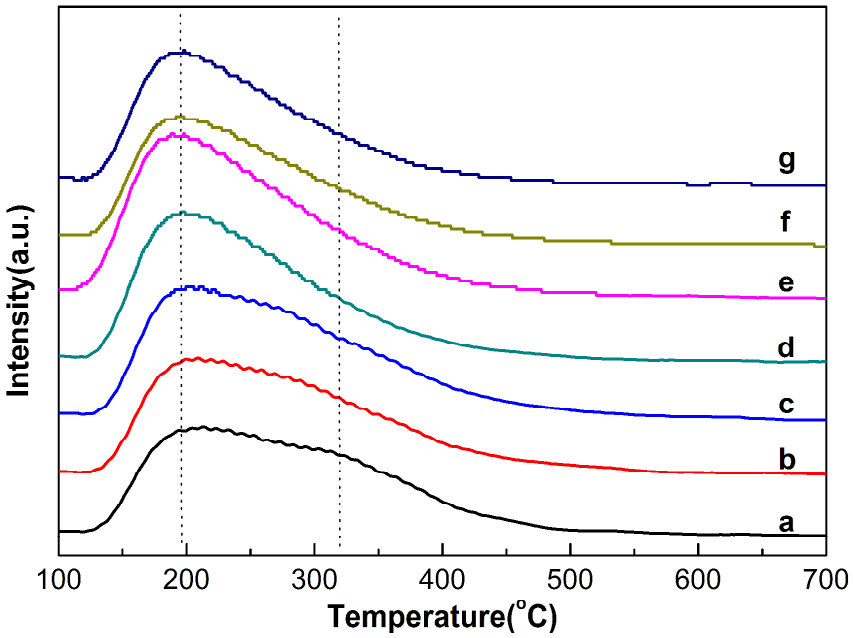


**Figure 11**

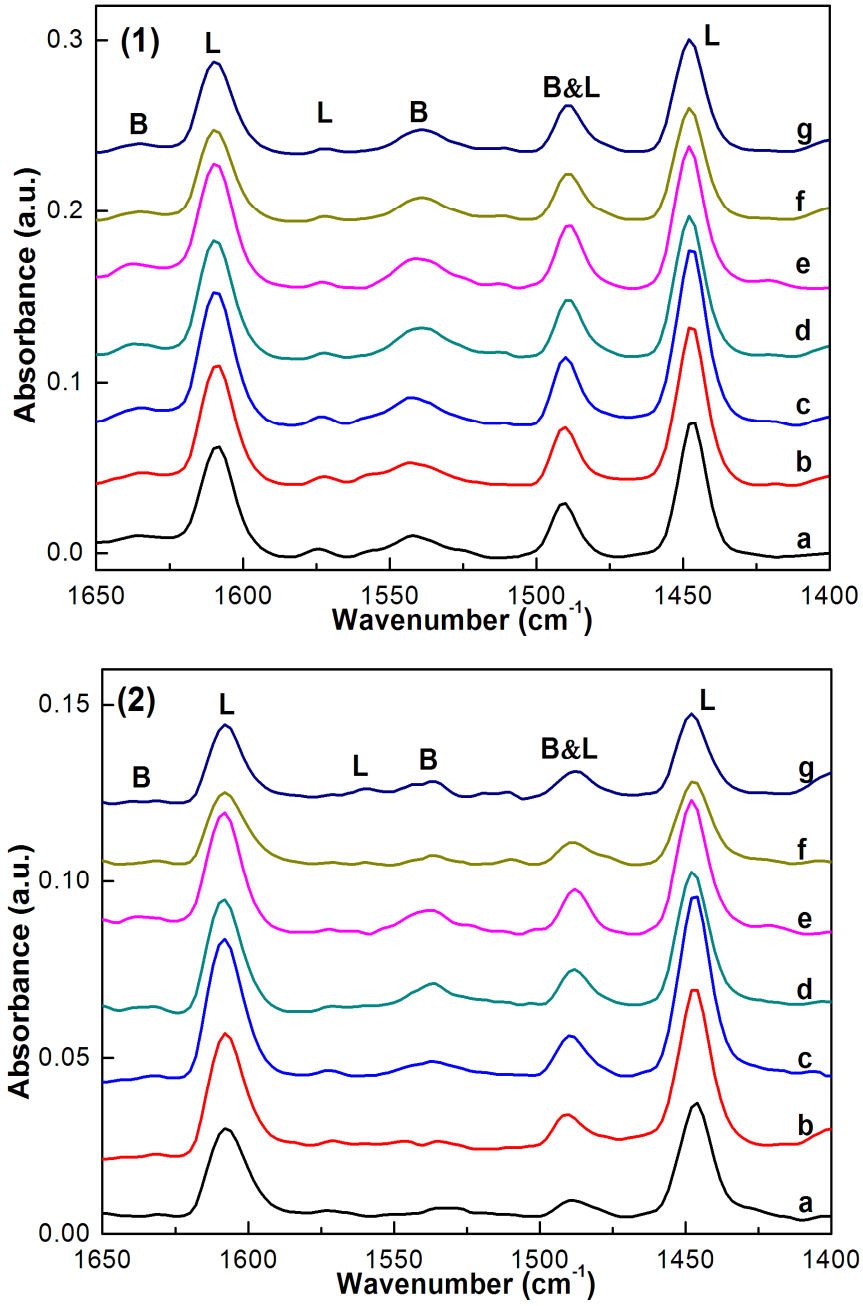


**Figure 12**

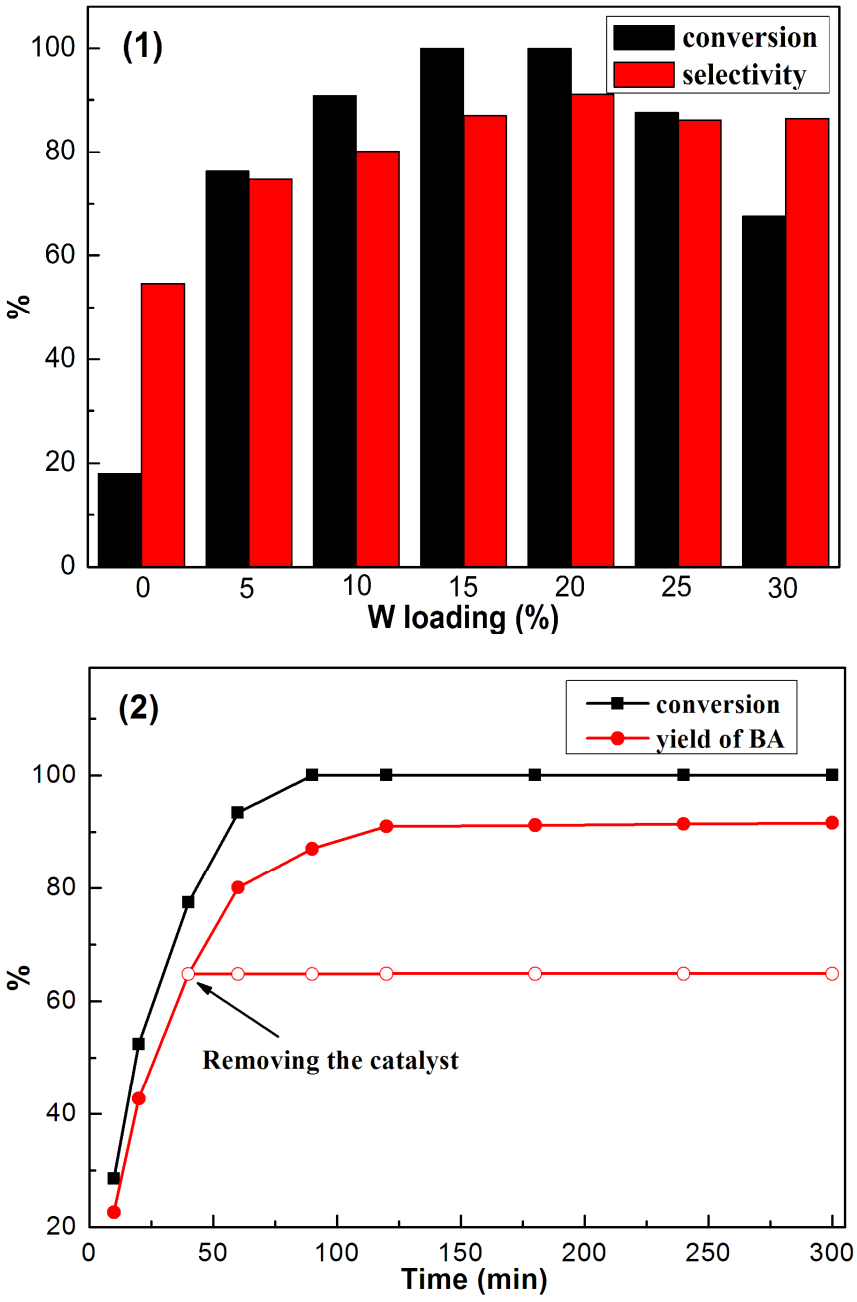


Figure 13

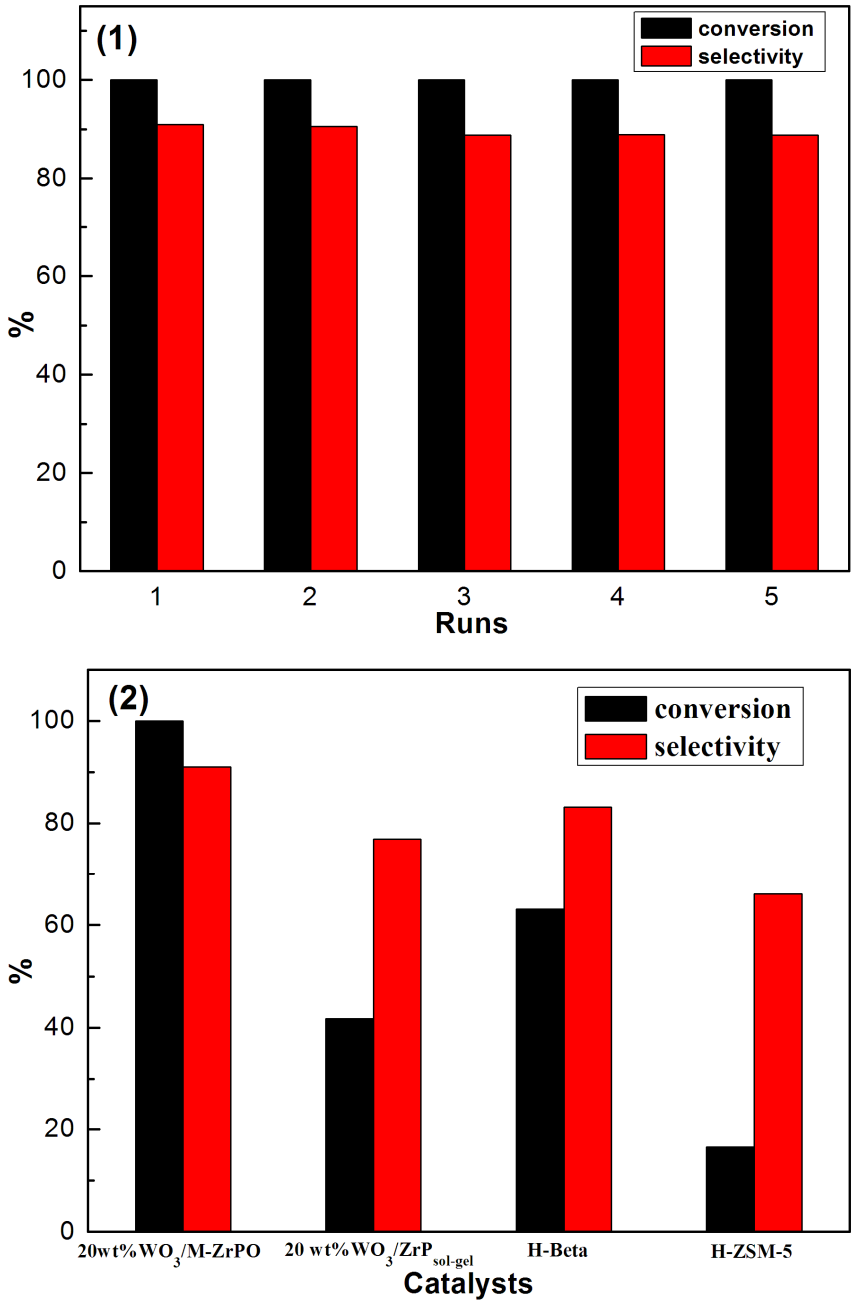


**Figure 14**

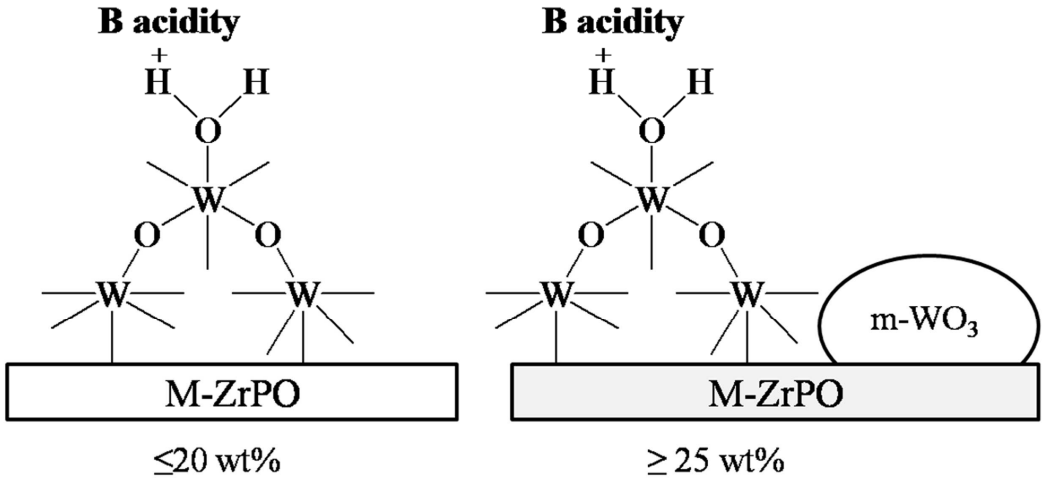


**Scheme 1**

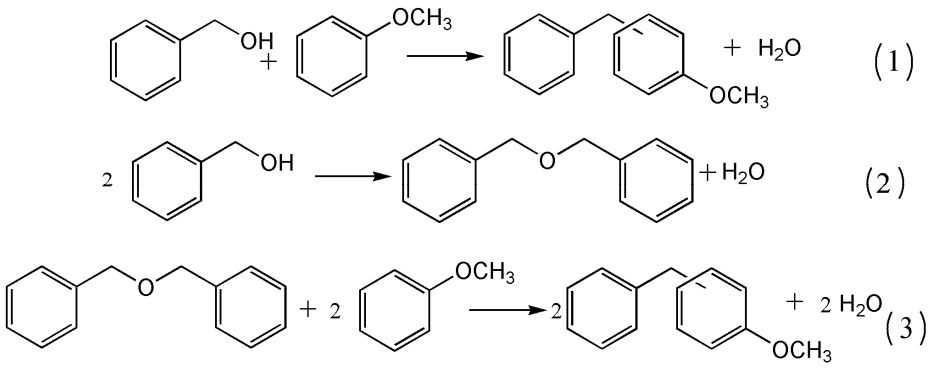


**Scheme 2**